Ambiguous resonances in multipulse quantum sensing with nitrogen-vacancy centers

Lucas Tsunaki,[1] Anmol Singh,[1] Kseniia Volkova,[1] Sergei Trofimov,[1] Tommaso Pregnolato,[2,3] Tim Schröder,[2,3] and Boris Naydenov[1,4,*]

[1]*Department Spins in Energy Conversion and Quantum Information Science (ASPIN), Helmholtz-Zentrum Berlin für Materialien und Energie GmbH, Hahn-Meitner-Platz 1, 14109 Berlin, Germany*

[2]*Department of Physics, Humboldt-Universität zu Berlin, Newtonstraße 15, 12489 Berlin, Germany*

[3]*Ferdinand-Braun-Institut (FBH), Gustav-Kirchhoff-Straße 4, 12489 Berlin, Germany*

[4]*Berlin Joint EPR Laboratory, Fachbereich Physik, Freie Universität Berlin, 14195 Berlin, Germany*

(Received 17 July 2024; revised 5 December 2024; accepted 27 January 2025; published 7 February 2025)

Dynamical decoupling multipulse sequences can be applied to solid-state spins for sensing weak oscillating fields from nearby single nuclear spins. By periodically reversing the probing system's evolution, other noises are counteracted and filtered out over the total evolution. However, the technique is subject to intricate interactions resulting in additional resonant responses, which can be misinterpreted with the actual signal intended to be measured. We experimentally characterize three of these effects present in single nitrogen-vacancy centers in diamond, where we also develop a numerical simulation model without rotating-wave approximation, showing robust correlation to the experimental data. Regarding centers with the ^{15}N nitrogen isotope, we observe that a small misalignment in the bias magnetic field causes the precession of the nitrogen nuclear spin to be sensed by the electronic spin of the center. Another studied case of ambiguous resonances comes from the coupling with lattice ^{13}C nuclei, where we use the echo modulation frequencies to obtain the interaction Hamiltonian and then utilize the latter to simulate multipulse sequences. Finally, we also measure and simulate the effects from the free evolution of the quantum system during finite pulse durations. Due to the large data volume and the strong dependence of these ambiguous resonances with specific experimental parameters, we provide a simulations data set with a user-friendly graphical interface, where users can compare simulations with their own experimental data for spectral disambiguation. Although focused on nitrogen-vacancy centers and dynamical decoupling sequences, these results and the developed model can potentially be applied to other solid-state spins and quantum sensing techniques.

DOI: 10.1103/PhysRevA.111.022606

I. INTRODUCTION

The second quantum revolution is driving sensing technology [1] to ever-increasing precision and accuracy, thus providing opportunities for novel measurement possibilities [2–9]. This quantum sensing advantage relies on the fact that quantum properties are extremely sensitive to their environment. However, such a key element is also a vulnerability, as quantum sensors are susceptible to complex interactions with their environment, leading to responses that can be misinterpreted with the actual signal intended to be measured.

In this study we consider these ambiguous resonant responses which affect multipulse dynamical decoupling (DD) pulse sequences. More specifically, the XY8-M [10,11] and other similar sequences are implemented, as schematically represented in Fig. 1(a). By periodically reversing the quantum evolution of the system with intercalated π_x and π_y pulses, dephasings from the environment are counteracted over the total evolution, thus making the sequence into a narrow filter for frequencies corresponding to double the pulse separation $f_0 = 1/2\tau$ and odd multiples thereof [12,13]: $3f_0, 5f_0, 7f_0, \ldots$. In such a manner, weak signals from single nuclear spins can be filtered from much stronger background fields even at room temperature [6–8], thus representing a remarkable improvement compared to conventional NMR, which requires large nuclear ensembles and much stronger bias magnetic fields. This improvement comes at the expense that the probing system is now intrinsically nonclassical; hence having knowledge of its time evolution is indispensable for the signal analysis. To overcome these challenges, an in-depth characterization of such ambiguous resonances experienced by the quantum sensor is necessary for the continued development of the field.

Despite being applicable to two-level systems in general, DD techniques excel with color center defects in solids [14], given their versatility to sense different physical quantities and relative ease of experimental realization. Among them, the nitrogen-vacancy (NV) center in diamond has been an epicenter of research due to its remarkable properties at a wide range of temperatures and compatibility with

*Contact author: boris.naydenov@helmholtz-berlin.de

Published by the American Physical Society under the terms of the Creative Commons Attribution 4.0 International license. Further distribution of this work must maintain attribution to the author(s) and the published article's title, journal citation, and DOI.

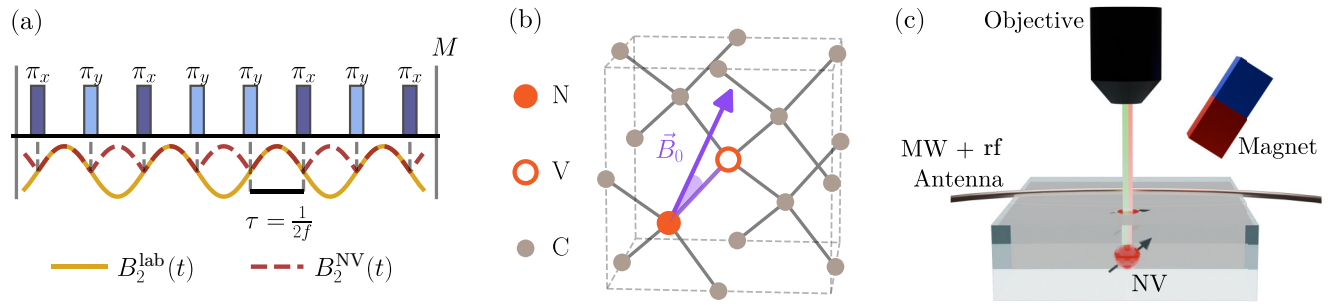

FIG. 1. (a) The XY8-M dynamical decoupling sequence is composed of eight alternating $\pi_{x,y}$ pulses repeated M times, which counteract oscillating magnetic-field noises except for frequencies corresponding to double pulse separation $f_0 = 1/2\tau$ and odd multiples of it. This sequence can be applied with a probing spin to sense weak oscillating fields from single nuclear spins. (b) The NV center is composed of a substitutional nitrogen adjacent to a vacancy in the carbon lattice of diamond. This results in an electronic spin triplet or singlet configuration, with well-defined quantum states within the band gap of diamond. In general, the external magnetic field $\vec{B}_0$ forms an angle θ_0 with the NV axis. ^{13}C isotopes with spin $\frac{1}{2}$ can also be present near the center. (c) Schematic representation of the experimental setup. An objective focuses the green laser to polarize the NV in the $m_s = 0$ state and collect its red fluorescence, which is used for the determination of the m_s state. The bias magnetic field $\vec{B}_0$ is applied with a permanent magnet, while microwave pulses for coherent control of the electronic spin are transmitted through a wire on top of the diamond.

biological systems [15,16], unlike, for instance, superconducting quantum interference devices [17]. Nitrogen-vacancy centers are a substitutional defect in the diamond lattice where a carbon atom is replaced by nitrogen ^{14}N ($I^n = 1$) or ^{15}N ($I^n = \frac{1}{2}$) adjacent to a vacancy [Fig. 1(b)]. In particular, the NV$^-$ (simply denoted by NV) attracts an extra electron from the lattice, forming a spin triplet configuration ($S = 1$), with well-defined quantum states within the band gap of diamond [18]. They can be efficiently polarized to the $m_s = 0$ state with a nonresonant green laser excitation via an optical pumping mechanism [19], which can also be used to read the population difference between $m_s = 0$ and ± 1 based on the resulting fluorescence. Finally, coherent transitions between the m_s states can be achieved by applying resonant microwave (MW) pulses with controllable phase and duration [20]. This way, a DD sequence consists of three parts: laser initialization, MW manipulation, and fluorescence readout. For NV centers, a $\pi/2$ pulse is included after the sequence, in order to drive the electronic spin to the quantization axis.

In the context of single NV multipulse sequences, ambiguous resonances can arise from different factors. We begin with Sec. II giving a general theoretical framework used in our simulations, following up with a description of the experimental and simulation methods in Sec. III. We then discuss the various ambiguous resonances appearing due to external magnetic-field misalignment and hyperfine interaction with ^{15}N nuclei (Sec. IV A), coupling with lattice ^{13}C having $I^c = \frac{1}{2}$ (Sec. IV B), or free evolution of the system during finite pulse duration [13] (Sec. IV C). In consideration of the numerous possible ambiguous resonances specific to experimental parameters, we conclude with Sec. V providing a data set with graphical interface where simulations can be visualized and compared with the user's experimental data for spectral disambiguation of resonances. Although the discussion is focused on NV centers, some of these effects are also relevant to other color centers and quantum systems in general.

II. THEORETICAL FRAMEWORK

In contrast to conventional NMR, in DD quantum sensing, the probing system is an inseparable part from the target spin and the exact Hamiltonian of the quantum sensor needs to be taken into account. The total Hamiltonian of an NV in a multipulse sequence can be decomposed into three parts as $H = H_0 + H_1(t) + H_2(t)$, where H_0 is the internal component, $H_1(t)$ is the control Hamiltonian describing the interaction with the MW pulses, and $H_2(t)$ is the sensing interaction itself. For the first internal component, we consider a spin model extensively studied and characterized [18,21,22]. It can be expressed in the Hilbert space of the electronic and nitrogen nuclear spins $\mathcal{H}_S \otimes \mathcal{H}_{I^n}$, in factors of decreasing energy as

$$\begin{aligned} H_0 = D&\left(S_z^2 - \frac{S^2}{3}\right) \\ &- \gamma^e \vec{B}_0 \cdot \vec{S} + a_\perp^n \left(S_x I_x^n + S_y I_y^n\right) \\ &+ a_\parallel^n S_z I_z^n \\ &- \gamma^n \vec{B}_0 \cdot \vec{I}^n, \end{aligned} \tag{1}$$

where the z axis is taken along the NV axis. The first line of Eq. (1) corresponds to the zero-field splitting due to the dipolar interaction between the two electrons, where $D = 2.87$ GHz is the axial component. The second and fourth lines correspond to Zeeman interactions with the external magnetic field $\vec{B}_0$ for the electronic spin and nitrogen nuclear spin, respectively, with gyromagnetic ratios $\gamma^e = -28\,025$ MHz/T, $\gamma^n = -4.316$ MHz/T for ^{15}N, and $\gamma^n = 3.077$ MHz/T for ^{14}N. Here we consider a general case where $\vec{B}_0$ is not necessarily aligned with the NV axis, as usually assumed. The third line is the hyperfine interaction between spins, which is diagonal in this symmetry reference frame, with $a_\perp^n = -2.70$ MHz and $a_\parallel^n = -2.14$ MHz for ^{14}N and $a_\perp^n = 3.65$ MHz and $a_\parallel^n = 3.03$ MHz for ^{15}N. When considering ^{14}N, there is an extra quadrupole term given by $Q(I_z^n)^2$, where $Q = -5.01$ MHz. Although small, the presence of the quadrupole interaction fundamentally changes the dynamics of the system, as the

interaction tends to fix the nuclear spin orientation and suppress the Larmor precession of ^{14}N nuclear spins for magnetic fields $B_0 \ll Q/\gamma^n = 1.63$ T [8].

The control Hamiltonian $H_1(t)$ for an oscillating field along a vector $\vec{B}_1$ with angular frequency $\Omega_{\rm MW}$ and phase ϕ_1 can be modeled as

$$H_1(t) = \gamma^e \sin(\Omega_{\rm MW} t + \phi_1)\vec{B}_1 \cdot \vec{S}. \tag{2}$$

Typically, a rotating-wave approximation (RWA) is assumed [23]. Thus, by setting the pulse frequency in resonance with one of the $m_s = 0 \leftrightarrow \pm 1$ transitions, $H_1(t)$ can be treated as a time-independent operator which induces a rotation on the Bloch sphere of the respective manifold, where the pulse duration controls the angle and ϕ_1 the axis of rotation in the rotating frame. Although this approximation often results in accurate descriptions of the electronic state transitions, it can overlook important interactions which lead to the ambiguous resonant responses. In particular, the $S_{x,y}$ components of the electronic Zeeman interaction and the perpendicular terms of the hyperfine interactions $a^n_\perp(S_x I^n_x + S_y I^n_y)$ do not commute with the rotation operator and result in extra resonances (Sec. IV A). This time dependence resulting from the noncommuting terms could still be handled as a perturbation to the secular part of the Hamiltonian up to the second order of the dominant term $(1/D)^p$ [8,24,25]. However, this approach is also limited, as it overlooks the possibility of double quantum transitions caused by multifrequency or broadband excitations [26], and it implies small bias fields $|\gamma_e \vec{B}_0| \ll D$ and weak driving regimes $\gamma_e B_1 \ll D$, which is not always experimentally desired due to extended pulse durations [27]. Furthermore, perturbation theory, in such circumstances, is restricted to calculating approximated eigenvalues for the perturbed Hamiltonian, ignoring exact characteristics of the MW field and the free evolution of the system during finite pulse durations, which also leads to other ambiguous resonances (Sec. IV C) [13].

For a single nuclear spin in the strong-coupling regime but without a contact term [9], the sensing Hamiltonian H_2 can be simply expressed in an extended Hilbert space to include the sensed target spin $\mathcal{H}_S \otimes \mathcal{H}_{I^n} \otimes \mathcal{H}_{I^c}$, where the sensed spin operator I^c denotes carbon nuclei for a concrete example. For a spin-$\frac{1}{2}$ target neglecting the interaction between the nitrogen and target nuclear spin, this Hamiltonian is given by a hyperfine coupling between the electronic spin operator and the sensed nuclear spin added to the Zeeman interaction with the external magnetic field

$$H_2 = \vec{S} \cdot A^c \cdot \vec{I}^c - \gamma^c \vec{B}_0 \cdot \vec{I}^c. \tag{3}$$

Diagonalizing the total Hamiltonian $H_0 + H_2$ results in distinct target nuclear spin Larmor frequencies $\tilde{\omega}^c_{m_s}$, dependent on the electronic spin state. Given that the hyperfine matrix A^c must be symmetrical, the sensing interaction is completely described by its six components plus the gyromagnetic ratio γ^c. The same Hamiltonian can also be used to describe an ensemble of nuclear spins, provided their states are represented by density operators. Apart from nuclear spins, it is also desirable to sense oscillating classical fields. Particularly for this study, an externally applied rf signal has the advantage of having controllable intensity and frequency. In this case, the interaction is described in terms of a field $\vec{B}_2(t)$ with frequency f_0 as

$$H_2(t) = \gamma^e \sin(2\pi f_0 t + \phi_2)\vec{B}_2 \cdot \vec{S}, \tag{4}$$

analogous to Eq. (2).

In a simplified manner, an ensemble of nuclear spins could also be thought of in terms of a semiclassical oscillating field [9,28]. Despite their average magnetization being close to zero at room temperature, their collective precession around $\vec{B}_0$ results in an effective oscillating magnetic field with statically varying amplitude and phase, but with frequencies centered around the effective nuclear Larmor frequencies $\tilde{\omega}^c_{m_s}$ at each electronic state m_s. On the other hand, a weak classical rf signal could emulate a precessing nuclear spin and be approximately described in terms of an effective hyperfine interaction. Hence, an analogy can be drawn between the quantum and semiclassical descriptions from Eqs. (3) and (4), where the interaction is represented in terms of either the six components of the three-dimensional symmetric hyperfine coupling matrix A^c_{ij} plus the gyromagnetic ration γ_s or the three nuclear precession frequencies $\tilde{\omega}^c_{0,\pm1}$ plus four parameters of the effective field vector ϕ_2 and $\vec{B}_0(x, y, z)$. Strictly speaking, both Hamiltonians describe fundamentally different processes, yet they share mathematical similarities and can lead to resembling effects at low-order XY8-M sequences, as shown further in Appendix E.

Altogether, a complete description of the pulsed dynamics of the NV subject to a multipulse sequence needs to account for the time-dependent MW pulses and oscillating rf field in the laboratory reference frame, while operating over mixed states. Within these considerations, the time evolution of the system can be solved by the Liouville–von Neumann equation

$$i\hbar\dot{\rho}(t) = [H_0 + H_1(t) + H_2(t), \rho(t)], \tag{5}$$

with $H_1(t)$ being present only during MW pulses but H_0 and $H_2(t)$ during the entire time evolution. This results in a set of coupled differential equations for the elements in the density matrix representing the whole system $\rho(t)$ [29], which can be integrated numerically in discretized small time steps [30,31]. Another advantage of this method is that nonunitary dynamics can be easily incorporated with the Lindblad equation [32], using the associated collapse operators of decoherence and relaxation. Finally, the observable measured after the DD sequence, i.e., the fluorescence, is given by the expectation value of the bright-state density operator $p = \mathrm{Tr}[\rho_0 \rho^\dagger(t_f)]$, where ρ_0 is the initial bright state and $\rho(t_f)$ the final state obtained from the equation. As discussed in Sec. I, the electronic spin is optically initialized at $m_s = 0$, while the nitrogen and target nuclear spins are in thermal equilibrium given by the Boltzmann distribution, which at room temperature leads to an identity density matrix. Thus, the initial state considered in the simulations is $\rho_0 \equiv |0\rangle\langle 0| \otimes \mathbb{1}^c \otimes \mathbb{1}^n$, where the dimensions of $\mathbb{1}$ depend on the spin of the nuclei.

III. EXPERIMENTAL AND SIMULATION METHODS

Experimental data are obtained with a homebuilt confocal microscope as described in [33,34] and schematically represented in Fig. 1(c). Single NV centers are addressed with a green laser in continuous or pulsed modes, while their fluorescence is measured by a single-photon detector. Microwave

pulses are produced by an arbitrary waveform generator and after amplification are transmitted to the diamond by a thin copper wire. Radio-frequency fields are generated continuously with controllable power and frequency, combined, and then transmitted without amplification with the already amplified MW pulses. The external bias magnetic field B_0 is applied with a permanent magnet with four degrees of movement, while its intensity and the angle formed with the NV axis θ_0 are calculated by the splitting asymmetry between peaks in the continuous wave or pulsed optical detected magnetic resonance (ODMR) spectrum [35]. Finally, the software package QUDI [36] is used for hardware control and data acquisition.

In order to study each ambiguous resonance, different properties are required for the measured diamond samples. For measuring ^{13}C ambiguous resonances in Sec. IV B, a chemical vapor deposition grown sample with ^{14}N is chosen in order to avoid ^{15}N effects. Conversely, in Sec. IV A, Hahn echo modulations and XY8-*M* are measured in shallow implanted ^{15}N diamonds. For longer XY8-12 measurements (Sec. IV C), a deeper implanted ^{15}N diamond sample is used with longer coherence times. A more detailed description of the experimental setup and diamond samples can be found in Appendices A and B.

The time evolution of the pulsed dynamics is calculated using the PYTHON package Quantum Color Centers Analysis Toolbox (QUACCATOO) [37], based on the master equation solver from Quantum Toolbox in PYTHON (QuTip) [30,31]. The most important simulations are open source and provided in the Example Notebooks section of the QUACCATOO package. Experimentally measured fluorescence and simulated transition probability are compared through a linear relation, physically representing experimental uncertainties, as the collection efficiency of the detection or background light. The correlation r between them is quantified from -1 to 1 by the Pearson coefficient [38] (see Appendix C for more details). In Sec. IV C, where the coupling parameters of H_2 are not defined, the transition probability is simulated over several points in parameter space and the simulation corresponding to the highest correlation coefficient is assumed.

IV. RESULTS

A. Magnetic-field misalignment and ^{15}N coupling

Perfectly aligning the bias field with the NV axis is typically only achievable using permanent magnets with precise rotating stages [24] or superconducting magnets. When considering manually controlled stages, as in our setup, the magnetic-field alignment is limited to about $\Delta\theta_0 = 1^\circ$. In these circumstances, the terms $S_{x,y}$ in the Zeeman interaction [see the first line of Eq. (1) and perpendicular nitrogen hyperfine terms can induce undesired electronic spin flips during multipulse sequences. This is better understood in another reference frame where $\vec{B}_0$ is aligned along its z axis, causing the nitrogen hyperfine matrix to assume nondiagonal terms just like in the sensing Hamiltonian of Eq. (3). Consequently, the misaligned field can cause the NV's electronic spin to sense its own nitrogen nuclear spin. Although this effect happens with both nitrogen isotopes, for ^{14}NV it is nearly negligible at moderate fields due to the quadrupole interaction (Sec. II); thus we restrict the discussion to ^{15}NV in this section.

The influence of ^{15}N coupling in simple pulsed experiments is already well known [39], resulting in an electron spin echo envelope modulation (ESEEM), as first observed by Rowan *et al.* [40] in electron paramagnetic resonance experiments. However, these approaches are restricted to a semianalytical framework [8,24] under certain approximations, as discussed in Sec. II. Here we show that the measured Hahn echo decay also agrees with our numerical simulation model with a high correlation of $r = 0.934$ [Fig. 2(a)]. The electronic coherence decay presents envelope modulations determined by the effective nitrogen Larmor frequencies $\tilde{\omega}^n_{m_s}$, as shown by the fast Fourier transform (FFT) taken from the simulated data [Fig. 2(b)]. However, as the number of pulses increases, an analytical approach for solving Eq. (5) and calculating this nitrogen coupling effect becomes increasingly complex.

To study these effects in longer DD sequences, XY8-2 for the $m_s = 0 \leftrightarrow +1$ transition was measured and simulated over a fixed τ range varying the magnetic-field intensity and orientation, as shown in Fig. 2(c). The frequency of nitrogen-related resonances does not depend linearly on the applied magnetic field, as one would expect from a simple Zeeman relation. In contrast, the hyperfine interaction, dominating the energy levels of the nuclei, results in peaks with varying intensity and nearly constant pulse separations as the field changes. The peak pulse separations do not correspond to the effective Larmor frequencies of the nitrogen nuclei $\tilde{\omega}^n_{m_s}$ and an analytical model which describes their resonant frequency values remains an open problem. The lowest magnetic field shows the worst correlation between experiment and simulation of $r = 0.858$, where a pulse duration error had to be included in the simulation. This causes a fast modulation of the signal, as discussed in detail in Appendix C. This smaller correlation can be attributed to a larger misalignment angle of $\theta_0 = 17.0^\circ$, thus with a larger uncertainty.

These resonances differ for each $m_s = 0 \leftrightarrow \pm 1$ transition due to distinct nuclear state energies and are also present at longer τ values given by the odd multiples of their resonant periods, as previously observed for ^{13}C resonances [6]. At long pulse separations of several microseconds, they mix and become a near continuum, which can be visualized in the simulations data set. ^{15}N resonances do not seem to occur at short pulse spacings of about less than 250 ns. Still, short τ are occupied by high-frequency noises from paramagnetic impurities and even fractions of the resonant periods (Sec. IV C) [13]. Moreover, setting the resonant frequencies of target nuclear spins with low gyromagnetic ratios γ^c at $\tau < 250$ ns is technically challenging, as it requires large bias fields B_0, additionally with broadband MW amplifiers for Ω_{MW} [Eq. (2)]. Thus, these resonances from ^{15}N are just unavoidable in many cases, underlying the necessity for a data set where users can compare their experimental data for disambiguation. It is important to note, however, that not all ^{15}NV centers under misaligned fields will present these ambiguous resonances, as additional interactions might dominate over it.

Figure 2(c) also illustrates how these resonances could be mistakenly attributed to some other nuclei. The ^{15}N resonance is compared with the expected Larmor frequency resonance

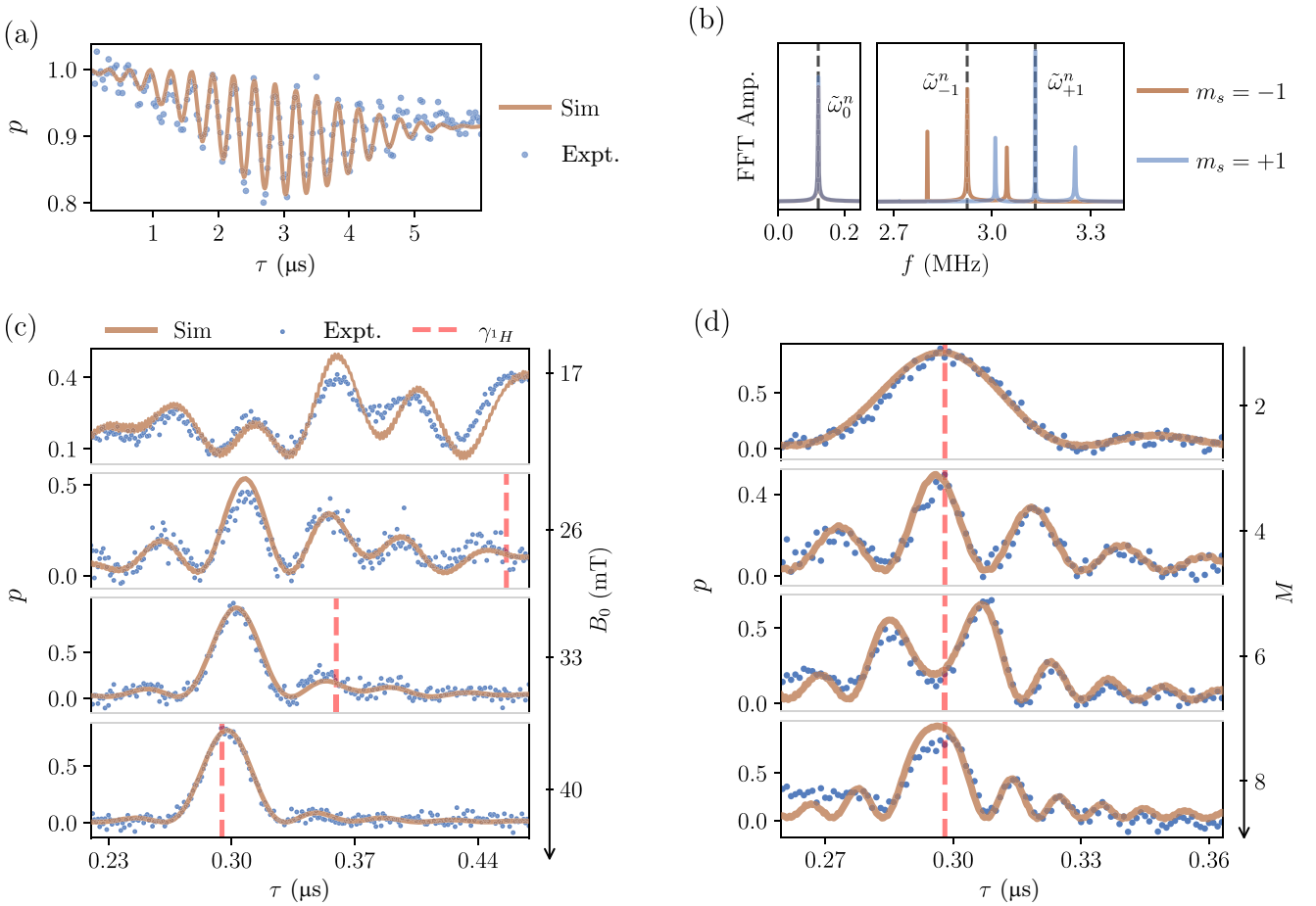

FIG. 2. (a) Experimental and simulated Hahn echo decay for the $m_s = 0 \leftrightarrow +1$ transition at $B_0 = 24$ mT and misalignment of $\theta_0 = 2.1°$. The field misalignment leads to the Larmor precession of the ^{15}N nuclear spin being sensed by the electronic spin of the NV center, resulting in the envelope modulations [8,24,39]. The coherence decay is fitted by $\exp[-(t/\tau_c)^4]$ [8], with $\tau_c = 4.018 \pm 0.007$ μs and correlation $r = 0.934$. The y axis represents the simulated transition probability p, while the experimental points are given by the fluorescence counts linearly fitted with the simulation data (Sec. III). This way, some of the experimental points appear above $p = 1$ due to experimental noise, even though this would be mathematically impossible. (b) FFT of the simulated Hahn echo decay for both $m_s = 0 \leftrightarrow \pm 1$ transitions. The envelope modulations are defined by the effective Larmor frequencies of ^{15}N $\tilde{\omega}^n_{m_s}$, numerically simulated from the Hamiltonian. Less intense sidebands from $\tilde{\omega}^n_{\pm 1}$ are also present in the spectra. (c) Experimental and simulated XY8-2 of the ^{15}N resonances for different values of B_0 with $\theta_0 = 17.0°$, 9.3°, 5.1°, and 2.7° and correlations $r = 0.858$, 0.890, 0.971, and 0.986, respectively. The resonance peaks have varying amplitude at almost constant pulse separations, evidencing a dominance of the hyperfine interaction with the electronic spin over the Zeeman interaction of the ^{15}N spin with $\vec{B}_0$. The expected resonances from ^{1}H are also shown at $\tau_H = 1/2\gamma_H B_0$. (d) XY8-M at $B_0 = 39$ mT and $\theta_0 = 2.6°$ with $r = 0.975, 0.921, 0.945, 0.906$. At this field, the ambiguous resonance could be mistakenly attributed to ^{1}H nuclear spins. The high correlation between simulations and experimental data for longer pulse sequences further corroborate the numerical model.

of the commonly measured ^{1}H nuclei $\tau_H = 1/2\gamma^h B_0$, where $\gamma^h = 42.57$ MHz/T. It can be seen that at 39 mT, the ambiguous resonance closely resembles a ^{1}H nucleus. In Fig. 2(d) the signal dependence on the order of the pulse sequence M is shown, while $B_0 = 39$ mT is kept constant. A strong agreement between the experimental data and the simulations is also observed for these longer sequences with many pulses, further corroborating the numerical model.

B. ^{13}C coupling

Carbon isotopes ^{13}C with nuclear spin $\frac{1}{2}$ are present in most diamonds with 1.1% natural abundance. ^{13}C sensing and manipulation by multipulse sequences is itself an active topic of research in consideration of the potential for long-lived quantum memories [6,41] and also for dynamic nuclear polarization applications [42,43], but in this case, it can act as another source of ambiguous resonances. Compared to ^{15}N in the preceding section, the Hamiltonian becomes more complex, as there are six free parameters from the hyperfine interaction A^c in Eq. (3) and off-diagonal terms cannot be assumed null because the reference frame is already being chosen such that $\vec{B}_0$ lies on the xz plane and the NV axis is along z. Therefore, the initial goal is to determine the hyperfine-interaction matrix A^c between an NV and a coupled ^{13}C nucleus such that the numerical simulations model can be validated with experimental data and subsequently extended to an arbitrary ^{13}C coupling or even other spins.

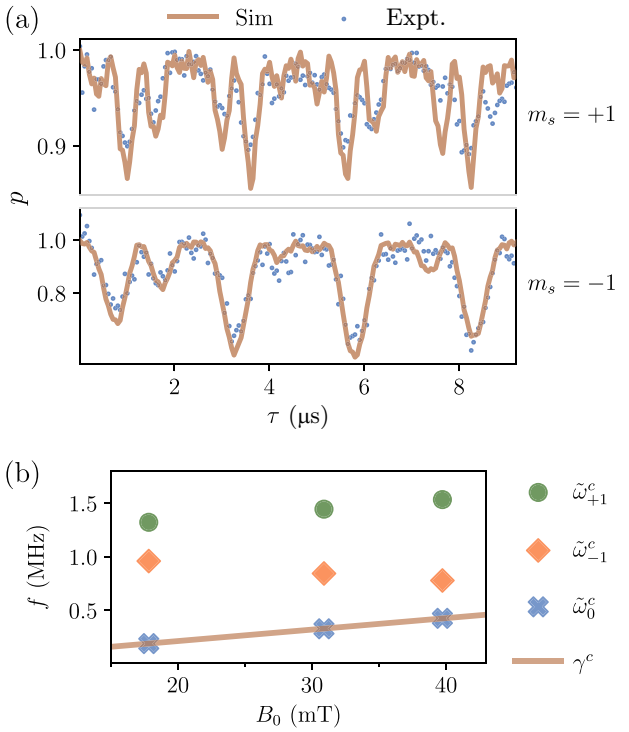

FIG. 3. (a) ESEEM measured with the Hahn echo sequence for both $m_s = 0 \rightarrow \pm 1$ transitions of a ^{14}NV coupled to a ^{13}C nuclear spin at $B_0 = 40$ mT. Both transitions show a slow modulation from the $\tilde{\omega}^c_0$ nuclear Larmor frequency at $m_s = 0$ and fast modulations $\tilde{\omega}^c_{\pm 1}$ from the $m_s = \pm 1$ states. Correlations between experimental and simulated data are $r = 0.761, 0.926$. As in Fig. 2(a), the experimental fluorescence linearly fitted with the simulated transition probability can reach values above $p > 1$ due to experimental noise. (b) Modulation frequencies obtained from the fit of the Hahn echo decay measurements as a function of B_0. Here $\tilde{\omega}^c_0$ is closely related to the bare gyromagnetic ratio of ^{13}C (solid line) due to an almost zero hyperfine interaction at $m_s = 0$, while $\tilde{\omega}^c_{\pm 1}$ also decreases or increases by the same amount with an offset given by Eq. (6). Error bars represented by the standard deviation from the fit are smaller than the points. Based on the experimental values of these modulations, the hyperfine tensor A^c was determined by comparing it with the calculated eigenvalues from the total Hamiltonian.

Similar to the coupling with ^{15}N, the Hahn echo decay of an NV coupled to a ^{13}C nuclear spin is also expected to show periodic oscillations given by the effective Larmor frequencies of the nuclei $\tilde{\omega}^c_{m_s}$ [8]. Thus, Hahn echo was measured in a single NV for both electron spin transitions $m_s = 0 \rightarrow \pm 1$ at three different magnetic fields, in a sample with the ^{14}N isotope to avoid nitrogen modulations as in the preceding section. The experimentally measured and later simulated modulations at $B_0 = 40$ mT are shown in Fig. 3(a), where no coherence decay can be observed at this timescale. The ESEEM for the two other values of B_0 can be found in Appendix D. As with ^{15}N coupling, the Hahn echo decay for the $m_s = 0 \rightarrow -1$ transition will present a slow modulation from $\tilde{\omega}^c_0$ and a fast one from $\tilde{\omega}^c_{-1}$, similar to the $m_s = 0 \rightarrow +1$ transition with $\tilde{\omega}^c_{+1}$ being the fast modulation. The values of the nuclear Larmor frequencies $\tilde{\omega}^c_{m_s}$ obtained from the fit of the curve [8] are plotted against the bias field in Fig. 3(b). The $\tilde{\omega}^c_0$ frequency is closely related to the bare gyromagnetic ratio of ^{13}C $\gamma^c = 10.705$ MHz/T, because of an almost zero hyperfine interaction at $m_s = 0$. On the other hand, $\tilde{\omega}^c_{+1}$ and $\tilde{\omega}^c_{-1}$ increase and decrease, respectively, by the same amount based on the sign of m_s. At $B_0 = 0$ mT, both of them are given by [44]

$$\tilde{\omega}^c_{\pm 1}(B_0 = 0) = \sqrt{\left(A^c_{zx}\right)^2 + \left(A^c_{zy}\right)^2 + \left(A^c_{zz}\right)^2}. \tag{6}$$

Finally, several different combinations of the hyperfine elements in Eq. (3) are considered and the eigenvalues of the total Hamiltonian $H_0 + H_2$ are calculated numerically. The hyperfine-interaction matrix A^c with the least-squares difference from the experimental values of $\tilde{\omega}^c_{m_s}$ is shown in Appendix D. Using the obtained A^c, the Hahn echo decay is simulated [Fig. 3(a)], resulting in the same experimental modulations with high correlations of $r = 0.761$ for $m_s = +1$ and $r = 0.926$ for $m_s = -1$.

Based on the obtained hyperfine-interaction matrix, the XY8-2 measurement for the $m_s = 0 \rightarrow +1$ transition is simulated and measured at the same bias magnetic fields, as shown in Fig. 4(a). The numerical simulation model and the calculated A^c accurately describe the resonances induced by the ^{13}C nuclear spin. As B_0 increases, the resonance shifts to shorter pulse separations and faster frequencies. This, in contrast to the coupling with ^{15}N [Fig. 2(c)], evidences that the Zeeman interaction of the ^{13}C nuclear spin with the external magnetic field is comparable in strength to the hyperfine interaction with the NV. Finally, Fig. 4(b) presents XY8-M measured and simulated at $B_0 = 40$ mT. Analogous to the ^{15}N resonance [Fig. 2(d)], the linewidth becomes narrower and sidebands become more pronounced as the order of the sequence increases, which can be understood in terms of an alteration of the frequency filter function induced by the DD sequence [28]. As the order increases, the correlation between experimental and simulation data decreases, possibly due to some pulse-length error (Appendix E) or inaccuracy in the fitted ESEEM frequencies.

At the magnetic fields shown here, this particular NV exhibits ^{13}C resonances which do not overlap with other possible nuclear spin species. However, for different couplings and fields, it may be the case that the interaction with ^{13}C leads to the appearance of ambiguous resonances mimicking other nuclear species. Given the crystalline periodicity of the host diamond, a ^{13}C atom can only occupy a limited number of lattice sites around the NV, resulting in a discrete set of possible hyperfine coupling strengths divided into families [44–46]. Thus, the data set provides simulations for hyperfine parameter values calculated from density-functional theory [44] such that a few possible ^{13}C resonances can be disambiguated from experimental data at different fields. A more conclusive method to identify the nuclear species giving rise to some resonance is however to measure ESEEM frequencies and compare the slow modulation with the expected gyromagnetic ratio, as performed here. Although we focus the discussion on lattice ^{13}C nuclear spins, the same method is applicable to an arbitrary spin coupled to the NV, as long as their interaction can be modeled by Eq. (3).

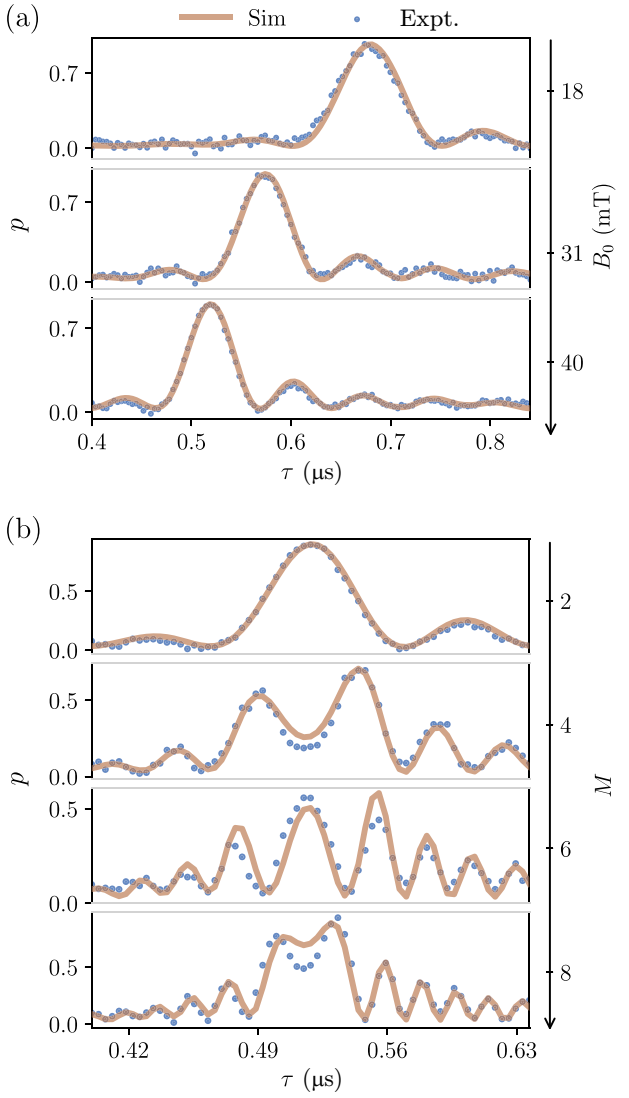

FIG. 4. (a) XY8-2 resonances from ^{14}NV coupled to a ^{13}C nuclear spin as a function of B_0 for the $m_s = 0 \rightarrow +1$ transition. The calculated hyperfine matrix A^c was used to simulate the resonances, with correlations $r = 0.987, 0.990, 0.989$. As the magnetic field increases, the resonance shifts to larger frequencies, influenced by the positive gyromagnetic ratio of ^{13}C. (b) Simulated and experimental XY8-M at $B_0 = 40$ mT, with correlations $r = 0.989, 0.977, 0.902, 0.951$. As the order of the sequence increases, sidebands become more pronounced and linewidths reduce due to changes in the filter function. For this ^{13}C coupling and these fields, these ambiguous resonances do not correspond to other nuclear spin. The high correlation between simulations and experiments attests to the robustness of the numerical model also in higher-dimensional Hilbert spaces, $\mathcal{H}_S \otimes \mathcal{H}_{I^n} \otimes \mathcal{H}_{I^c}$.

C. Finite pulse duration

In most applications of multipulse sequences, perfect δ pulses with zero temporal length are assumed. Even though the pulse length might still be much smaller than the pulse separation $t_\pi \ll \tau$, it has been shown that the free evolution of the system during finite pulse durations under the influence of H_0 leads to additional resonances at even multiples of the resonant frequencies and their odd subharmonics [13], that

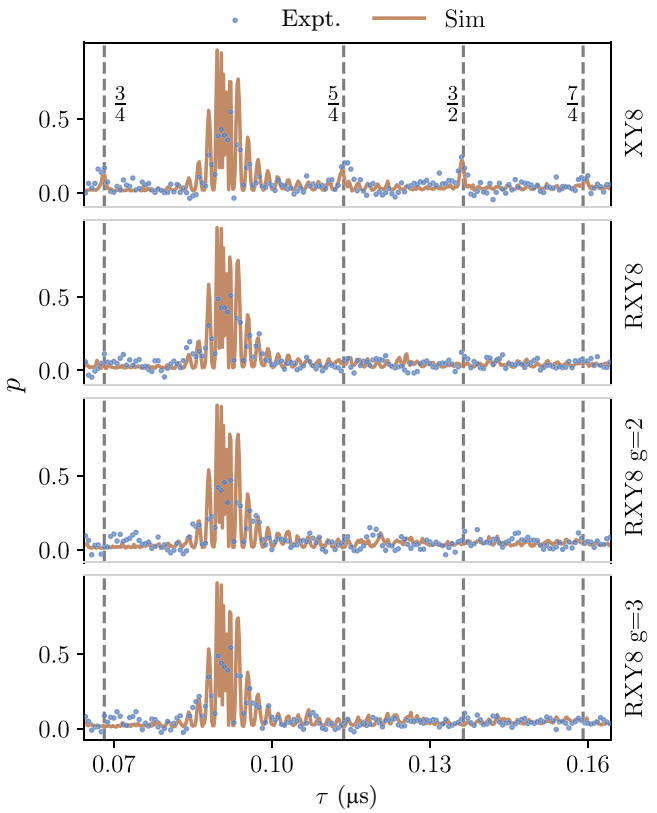

FIG. 5. The XY8-12 and RXY8-12 sequences with resonance from an external rf signal with $f_0 = 5.5$ MHz for the $m_s = 0 \leftrightarrow -1$ transition. Multiple fringes are observed around the fundamental resonance $\tau_0 = 1/2f_0$. In addition, spurious harmonics due to the finite pulse length at $\tau/\tau_0 = \frac{3}{4}, \frac{5}{4}, \frac{3}{2}$, and $\frac{7}{4}$ are suppressed by the phase randomization [47,48]. A proposed improvement of the RXY8 sequence by random-phase correlations with $g = 2$ and 3 [49] is also demonstrated, without significant differences from uncorrelated RXY8, thus indicating that phase correlation can be introduced in the RXY8 sequences without affecting nonspurious spectral features. The best correlations $r = 0.839, 0.877, 0.818, 0.888$ occur at $\gamma_e B_2^x = 0.28$ MHz and $\gamma_e B_2^y = \gamma_e B_2^y = 0$ from Eq. (4).

is, $\tau = (2k+1)/2l\tau_0$ for k and l natural. Notably, lattice ^{13}C nuclear spins can give rise to such spurious harmonics which could be mistakenly attributed to ^{1}H, apart from the ambiguous resonances discussed in Sec. IV B. This occurs because the fourth harmonic of a weakly coupled ^{13}C coincides with the fundamental resonance of ^{1}H, given that $4\gamma^c = 42.82$ MHz/T and $\gamma^h = 42.57$ MHz/T. These spurious resonances can still be greatly suppressed by adding a random phase Φ_m for each XY8$_m$ block, known as the RXY8-M sequence [47,48]. A further improvement of this suppression was theoretically proposed by correlating the random phases such that they cancel each other every g repetitions of the XY8 block, $\sum_m^g \exp(-i\Phi_m) = 0$ [49].

To experimentally reproduce these spurious resonances, an external rf signal with frequency $f_0 = 5.5$ MHz is applied to a single NV at bias field $B_0 = 38$ mT, where the MW π-pulse length is $t_\pi = 17.16$ ns. Four different multipulse sequences are applied as shown in Fig. 5. In all four we observe multiple fringes around the fundamental resonance $\tau_0 = 1/2f_0$,

resulting from the convolution of the spectral density of the rf field and the filter function of the multipulse sequence [28]. Apart from that, XY8-12 has four of these spurious resonances at $\tau/\tau_0 = \frac{3}{4}, \frac{5}{4}, \frac{3}{2}$, and $\frac{7}{4}$, which are almost entirely suppressed with RXY8-12. Furthermore, we demonstrate the experimental realization of RXY8-12 with correlated phases at $g = 2$ and 3 repetitions. At these experimental conditions, the two sequences show no noticeable differences from uncorrelated RXY8, meaning they can be used instead of the RXY8, as they have additional robustness against pulse errors [49], such as in the pulse length and detuning of the MW resonant frequency. These lead to a degradation of the resonance contrasts and are discussed in more detail in Appendix E.

Equation (4) was used to model the rf interaction with the NV, with the best correlations found for $\gamma_e B_2^z = 0.28$ MHz and $\gamma_e B_2^x = \gamma_e B_2^y = 0$. The simulations also show a suppression of the spurious harmonics by the phase randomization, hence demonstrating that the numerical simulation model can be applied for time-dependent sensing Hamiltonians $H_2(t)$ while also taking into account the specific time dependence of the control Hamiltonian $H_1(t)$ from Eq. (2).

V. DISCUSSION AND SIMULATIONS DATA SET

Noise filtering by DD sequences has proven to be an effective technique in quantum sensing, capable of detecting very weak oscillating fields of even single nuclear spins. This great sensitivity comes at the cost of a complex signal analysis influenced by external and inherent interactions which lead to ambiguous resonances, such as the ones studied here. It is therefore imperative that these effects are well understood and characterized for an accurate identification of nuclear spin resonances. Among candidate platforms, the NV center in diamonds stands out in its ease of implementation and versatility with different biological and chemical systems. Nevertheless, widely adopted approximations and oversimplifications of the system dynamics completely overlook these ambiguous resonances. Examples of such approximations are the RWA, assuming perfect δ pulses, adopting a reduced electronic spin manifold where $S = \frac{1}{2}$ or ignoring the nitrogen nuclear spin of the NV.

In this work we presented a numerical simulations model for the time-dependent dynamics of the NV under a DD sequence and experimentally characterized three effects that lead to ambiguous resonances. First, in ^{15}NV centers, a small misalignment of $\vec{B}_0$ causes the precession of ^{15}N nuclear spins to be sensed via the hyperfine interaction. As demonstrated here, these resonances can closely resemble a ^{1}H nuclear spin. Another relevant source of ambiguous resonances are the diamond lattice ^{13}C nuclear spins, which also couple to the NV electronic spin through the hyperfine-interaction matrix A^c. Here we have presented a method for unequivocally calculating A^c, based on the ESEEM frequencies as a function of the bias field B_0. This method can be generalized to any coupled spins in the strong-coupling regime [9], which can be expressed in terms of a Hamiltonian as in Eq. (3). Finally, specific parameters of the MW control pulses which are not accounted for in perturbation theory also affect the resonances of DD sequences. In particular, the free evolution of the probing spin during finite pulse durations leads to resonances at the even fractions of the fundamental resonant periods [13]. These resonances can be suppressed with phase randomization in each XY8 block [47,48], where we experimentally demonstrated a proposed improvement with random-phase correlation [49].

Unlike the spurious resonances originating from the finite pulse durations, a straightforward method for suppressing the ambiguous resonances from ^{15}N and ^{13}C remains a problem. Currently, this would involve more elaborate experimental conditions, such as precise vector magnets, isotopically purified diamonds, or more complicated pulse sequences. Another important technique that can be potentially employed for improving pulse fidelity and could compensate for finite-length hard pulses is pulse shaping [50], which could be easily incorporated in our numerical simulations model. In conclusion, some of the ambiguous resonances presented here are simply unavoidable in a large variety of experiments. A platform for analyzing and identifying spectral features is thus essential for the continued development of the field, as these ambiguous resonances are largely dependent on specific experimental parameters, resulting in numerous possible resonant responses in multipulse DD sequences.

To further extend the toolbox of available methods, we provided a data set comprised of around 10^4 simulations of XY8-M for ^{15}N and ^{13}C ambiguous resonances. Both m_s transitions were considered with several different combinations of B_0 and order M. It is important to note, however, that a fixed Rabi frequency of $\gamma_e B_1 = 40$ MHz was considered in all simulations of the data set, which may lead to slight differences at high-order XY8. This typically high Rabi frequency was chosen in order to mitigate the spurious resonances from finite pulse durations and thus not overlap it with the two other sources of ambiguous resonances. Nonetheless, QUACCATOO [37] provides the necessary tools for simulating arbitrary MW fields. For ^{15}N resonances, the angle θ_0 was changed, whereas for ^{13}C, the hyperfine matrices of all provided families [44] were considered. The simulations can be visualized and compared with the user's experimental data for spectral disambiguation through an open source and user-friendly graphical interface, available in [51], where a complete guide for installation and usage are also provided. Even though the data set only contains XY8-M simulations for NV centers, it can be used for other sequences which have similar resonance spectra, such as the Carr-Purcell-Meiboom-Gill sequence [10].

In the ambiguous resonances studied here, the simulations model presented robust correlations with the experimental data. Numerically solving the system's time-dependent dynamics without the RWA has proven to be a more versatile and robust approach than semianalytical models, e.g., perturbation theory. Although primarily focused on NV centers, the developed model can be applied to any quantum system that satisfies the following three criteria: It can be described in terms of the density matrix formalism, it has a total Hamiltonian that can be divided in three parts as $H = H_0 + H_1(t) + H_2(t)$, and it has a Hermitian observable. Most color centers and many other quantum systems satisfy

these conditions. Furthermore, the generality of $H_1(t)$ implies that the model can be extended to more elaborate DD sensing protocols as well.

ACKNOWLEDGMENTS

We acknowledge Miriam Mendoza Delgado and Dr. Cyril Popov from the Institute of Nanostructure Technologies and Analytics of the University of Kassel for annealing a diamond sample. We are also grateful to Karolina Schüle, Jens Fuhrmann, and Dr. Fedor Jelezko from the Institute for Quantum Optics of Ulm University for providing another diamond sample. Finally, we would like to thank Alexander Külberg and Dr. Andreas Thies from Ferdinand-Braun-Institute (FBH) for performing the ion implantations. This work was supported by the German Federal Ministry of Education and Research (BMBF) under the Grand Challenge of Quantum Communication, in a collaboration between the projects DIamant-basiert QuantenTOKen (DIQTOK) (Project No. 16KISQ034) and Quantum Photonic Integrated Scalable memory (QPIS) (Project No. 16KISQ032K). In addition, this work received funding from BMBF project DiNOQuant (No. 13N14921) and German Research Foundation (DFG) Grants No. 410866378 and No. 41086656.

DATA AVAILABILITY

All data used in this work are available for scientific use upon reasonable request.

All code used in this work is available for scientific use upon reasonable request.

APPENDIX A: EXPERIMENTAL SETUP AND DATA ACQUISITION

The experiments were performed on a custom-made confocal microscope. The diamond samples were mounted on a custom-made three-dimensional stage movable with 10 µm precision. A diode laser with a wavelength of 518 nm (iBEAM-SMART-515-S, TOPTICA Photonics AG) was used for both continuous and pulsed optical excitation of an NV center. In deeper implanted NV samples, emitted fluorescence was collected with an oil objective (HCX PL APO 100 × /1.40, Leica; type F immersion liquid, Leica) with numerical aperture of 1.40, in order to improve collection efficiency. Conversely, in shallow samples, an air objective (MPlanApo N 50 × /0.95, Olympus) with a numerical aperture of 0.95 was used to avoid nuclear spin signals from the oil. In either case, the photons were detected by an avalanche photodiode (SPCM-AQRH-14, Excelitas). The objective was mounted on a piezoelectric scanner (P-517, Physikinstrumente) with subnanometer resolution. The laser light was blocked from entering the detector by a 650 nm longpass filter (FELH0650, Thorlabs). A continuous MW field for ODMR spectra was generated by a microwave source (TGR6000, TTi) and the rf signal in Sec. IV C by a function generator (TGF4242 LXI, TTi). Microwave pulses for dynamical decoupling multipulse sequences were generated by an arbitrary waveform generator (AWG7122C, Tektronix), with maximum sampling frequency of 12 GSamples/s and memory of 64 MSamples. In both cases, generated MW fields were amplified (ZHL-16W-43+, MiniCircuit) and combined with the nonamplified rf using a bias tee (Mini Circuits, ZABT-2R15G+). Finally, they were transmitted to the NV centers by a copper (99.99%) wire with a diameter of 20 µm. The bias magnetic field was applied with a permanent magnet mounted on a holder with four degrees of freedom and with the maximum achievable magnetic-field projection on the NV center axis of 0.1 T. For time-resolved photon counting we used a time-correlated single-photon counter (MCS6, FAST ComTec). Prior to all pulsed measurements, the π-pulse duration was measured with a Rabi sequence. The experimental value of the Rabi frequency was then used in the simulations. Finally, laser pulses for state polarization and readout were applied for 3 µs and power from 0.1 to 0.5 mW, depending on the sample. The pulsed experiments conducted here are thoroughly discussed in Ref. [28].

APPENDIX B: DIAMOND SAMPLES

In Sec. IV A, the effects of ^{15}N coupling on Hahn echo were measured in a IIa diamond with a ^{12}C overgrown layer of 90 nm, which was later implanted with ^{15}N at an energy of 2 keV and annealed at 1000 °C in ultrahigh vacuum. For the XY8-M measurements, another shallow implanted sample was used with an implantation energy of 2 keV and dose of 10^9 $^{15}N^+/cm^2$, annealed at 10^{-7} mbar and 1000 °C. In Sec. IV B, the ^{13}C ambiguous resonance were studied in an

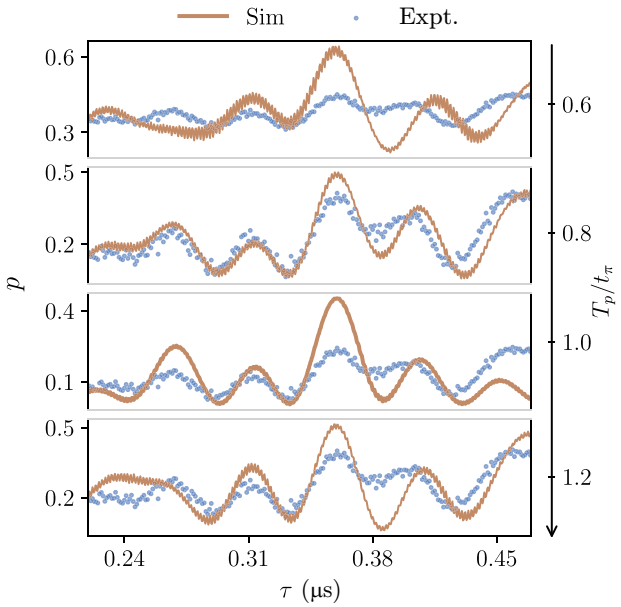

FIG. 6. The XY8-2 sequence of the ambiguous ^{15}N resonance (Sec. IV A) as a function of the pulse duration T_p/t_π exemplifies the use of the Pearson coefficient, with $r = 0.419$, 0.858, 0.555, and 0.685 for $T_p/t_\pi = 0.620$, 0.826, 1.000, and 1.215, respectively. At $T_p/t_\pi = 1$ the simulated and experimental data have a poor correlation, but considering a small deviation, the experimental data can be better modeled by the simulation. The pulse error induces a high-frequency modulation of the signal and variations in the peak intensities.

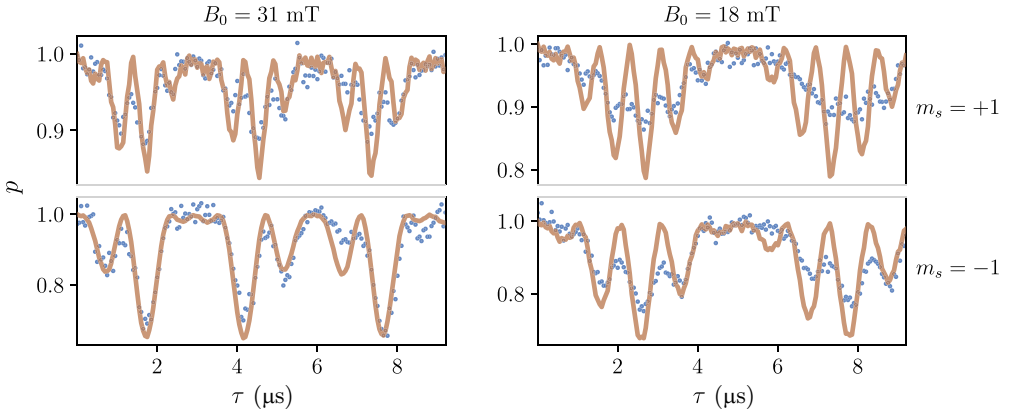

FIG. 7. Hahn echo modulations from a ^{14}NV coupled to a ^{13}C nuclear spin, resulting in correlations between experimental and simulated data of $r = 0.792, 0.925$ at $B_0 = 31$ mT and $r = 0.659, 0.806$ at $B_0 = 18$ mT. Although both agree in terms of the modulation frequencies, the amplitude of the faster modulation is smaller in the experimental data, which could be due to some experimental error or unconsidered factor in the Hamiltonian.

electronic grade diamond grown by chemical vapor deposition, with natural abundance of ^{13}C and ^{14}N, in order to avoid ^{15}N effects. Finally, the ambiguous resonances from finite pulses in Sec. IV C were measured in a thin electronic grade diamond plate with deeper ^{15}N implantation (20–30 keV) and doses around 10^9 $^{15}N^+/cm^2$, also annealed in ultrahigh vacuum at 1000 °C.

APPENDIX C: PEARSON CORRELATION COEFFICIENT

As discussed in Sec. III, experimental fluorescence intensity and simulated transition probability to the bright state ($m_s = 0$) are related through a linear equation. Therefore, an appropriate metric to determine the correlation between both is the Pearson coefficient r [38], which is the square root of the coefficient of determination R^2 for linear relations. It is defined as the ratio between the covariance of the two data sets and the product of their standard deviations, where one data set represents the experimental data and the other the simulation. Within this definition, r is normalized from -1 to 1, with $r = 0$ representing no linear dependence between experimental and simulated data, while $r = 1$ indicates a perfect linear correlation.

To illustrate this, Fig. 6 shows simulations for XY8-2 of the ^{15}N ambiguous resonances at $B_0 = 17$ mT for different pulse length deviations in regard to the actual π-pulse duration T_p/t_π (Sec. IV A). Compared to the actual experimental data, assuming $T_p/t_\pi = 1$ results in a low correlation of $r = 0.555$ and thus an inadequate simulation of the experimental data, whereas taking $T_p/t_\pi = 0.826$ provides a better correlation of $r = 0.858$. In this case, the pulse length deviation affects the relative intensity of each resonance peak keeping their τ fixed while also inducing a high-frequency modulation of the signal.

APPENDIX D: ^{13}C HAHN ECHO MODULATIONS

The ESEEMs measured by a Hahn echo sequence at $B_0 = 31$ and 18 mT for both m_s transitions are shown in Fig. 7. As observed, the simulations and experimental data both present the same modulation frequencies; however, the amplitude of the fast modulation is smaller in the experiments. This could be related to some experimental error or some unconsidered factor in the Hamiltonian model. Nonetheless, this discrepancy does not affect the study of the ambiguous resonances and, as seen in Sec. IV B, the calculated hyperfine matrix and the numerical model still reliably described them.

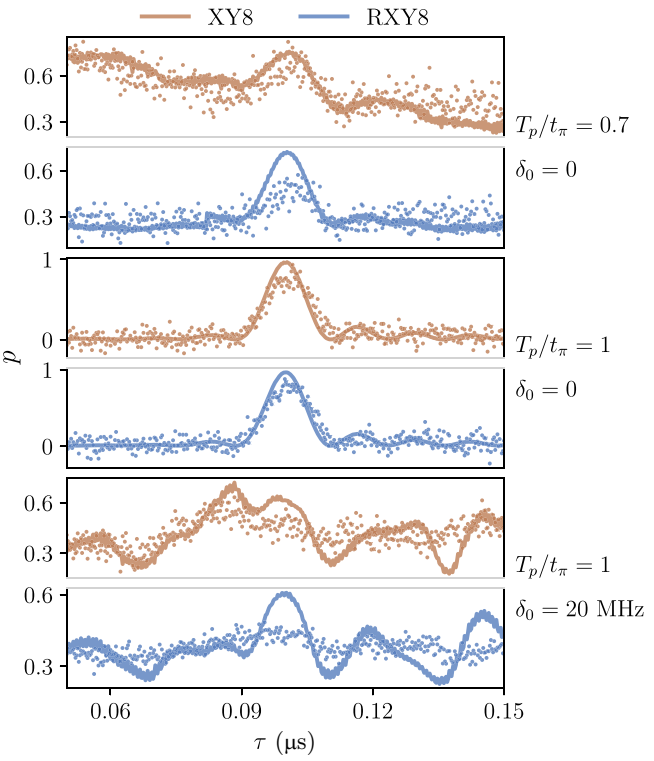

FIG. 8. The XY8-2 and RXY8-2 sequences with an external rf signal of $f_0 = 5$ MHz with MW pulse deviation of $\delta_0 = 20$ MHz or length error of $T_p/t_\pi = 0.7$. The rf field is approximated by an effective hyperfine coupling with $A^s_{xz} = 0.92$ MHz, resulting in $r = 0.763, 0.907, 0.626$ for XY8-2 and $r = 0.639, 0.915, 0.423$ in RXY8-2. The pulse errors lead to a degradation of the contrast and additional resonances, which are suppressed by the random phases.

Based on those experimental values of the modulation frequencies, different combinations of hyperfine coupling matrices between the NV and the ^{13}C nuclear spin were tested in the total Hamiltonian $H_0 + H_2$ from Eqs. (1) and (3). The eigenenergies of the Hamiltonians were calculated numerically, with the effective Larmor frequencies $\tilde{\omega}^c_{m_s}$ corresponding to the energy differences between the carbon nuclear spin states in each electron spin state m_s. Since no splittings could be observed in the two m_s resonances, the ODMR spectrum sensitivity sets an upper bound for the $|A^c_{zz}|$ component of 4 MHz. Furthermore, the nondiagonal components of the ^{13}C families are lower or of the same order as $|A^c_{zz}|$ [44]; thus this bound was also assumed for the remaining components of A^c. Initially then, the six hyperfine elements were linearly varied in the interval from -4.0 to 4.0 MHz with a large spacing of 0.5 MHz. Having found an approximate optimal region of the parameter space, each parameter was subsequently varied with spacing 0.01 MHz in this smaller range, totaling over 10^7 possible combinations. Ultimately, the hyperfine matrix with the least-squares difference in units of megahertz was found to be

$$A^c = \begin{pmatrix} -0.25 & -1.85 & -0.49 \\ -1.85 & 0.00 & 0.01 \\ -0.49 & 0.01 & 1.01 \end{pmatrix}.$$

APPENDIX E: PULSE ERRORS

Phase randomization can greatly increase robustness against pulse errors [47,49]. In nonrandomized XY8, small detunings in the MW frequency δ_0 and deviations in the pulse length T_p/t_π lead to a degradation of the resonance contrast and additional peaks over the τ range, which could represent another source of an ambiguous resonance for similar frequency rf fields or spins. To show this effect, XY8-2 and RXY8-2 with uncorrelated phases were measured and simulated with an applied rf field of $f_0 = 5$ MHz, taking $\delta_0 = 20$ MHz and $T_p/t_\pi = 0.7$ separately (Fig. 8). Experimental parameters are $t_\pi = 15.24$ ns and $B_0 = 34$ mT with $\theta_0 = 4.1^\circ$. Again, we observe a suppression of the spurious peaks in RXY8-2 and a further validation of the simulation model. In this case at low order $M = 2$, the rf signal can be approximated by an effective hyperfine interaction with $A^s_{xz} = 0.92$ MHz and $\gamma^s B_0 = 5$ MHz, as in Eq. (4), whereas for the higher-order XY8-12 from Sec. IV C, the quantum-mechanical approximation of the classical rf field already deviates from the experimental data. At the large detuning considered here $\delta_0 = 20$ MHz, the simulation shows smaller correlation with the experimental data. This evidences a limitation of the numerical model, while the reasons for it remain an open problem. Nonetheless, such large detuning might not be of practical significance for most experiments, apart from benchmarking the numerical simulations model.

[1] C. L. Degen, F. Reinhard, and P. Cappellaro, Quantum sensing, Rev. Mod. Phys. **89**, 035002 (2017).

[2] B. P. Abbott *et al.*, GW150914: The advanced LIGO detectors in the era of first discoveries, Phys. Rev. Lett. **116**, 131103 (2016).

[3] S. Chen *et al.*, Immunomagnetic microscopy of tumor tissues using quantum sensors in diamond, Proc. Natl. Acad. Sci. USA **119**, e2118876119 (2022).

[4] N. Aslam, H. Zhou, E. K. Urbach, M. J. Turner, R. L. Walsworth, M. D. Lukin, and H. Park, Quantum sensors for biomedical applications, Nat. Rev. Phys. **5**, 157 (2023).

[5] M. Fujiwara, S. Sun, A. Dohms, Y. Nishimura, K. Suto, Y. Takezawa, K. Oshimi, L. Zhao, N. Sadzak, Y. Umehara, Y. Teki, N. Komatsu, O. Benson, Y. Shikano, and E. Kage-Nakadai, Real-time nanodiamond thermometry probing in vivo thermogenic responses, Sci. Adv. **6**, eaba9636 (2020).

[6] T. H. Taminiau, J. J. T. Wagenaar, T. van der Sar, F. Jelezko, V. V. Dobrovitski, and R. Hanson, Detection and control of individual nuclear spins using a weakly coupled electron spin, Phys. Rev. Lett. **109**, 137602 (2012).

[7] P. Neumann, J. Beck, M. Steiner, F. Rempp, H. Fedder, P. Hemmer, and F. Jelezko, Single-shot readout of a single nuclear spin, Science **329**, 542 (2010).

[8] L. Childress, M. V. Gurudev Dutt, J. M. Taylor, A. S. Zibrov, F. Jelezko, J. Wrachtrup, P. R. Hemmer, and M. D. Lukin, Coherent dynamics of coupled electron and nuclear spin qubits in diamond, Science **314**, 281 (2006).

[9] C. Müller, X. Kong, J.-M. Cai, K. Melentijević, A. Stacey, M. Markham, D. Twitchen, J. Isoya, S. Pezzagna, J. Meijer *et al.*, Nuclear magnetic resonance spectroscopy with single spin sensitivity, Nat. Commun. **5**, 4703 (2014).

[10] S. Meiboom and D. Gill, Modified spin-echo method for measuring nuclear relaxation times, Rev. Sci. Instrum. **29**, 688 (1958).

[11] B. Naydenov, F. Dolde, L. T. Hall, C. Shin, H. Fedder, L. C. L. Hollenberg, F. Jelezko, and J. Wrachtrup, Dynamical decoupling of a single-electron spin at room temperature, Phys. Rev. B **83**, 081201(R) (2011).

[12] G. de Lange, D. Ristè, V. V. Dobrovitski, and R. Hanson, Single-spin magnetometry with multipulse sensing sequences, Phys. Rev. Lett. **106**, 080802 (2011).

[13] M. Loretz, J. M. Boss, T. Rosskopf, H. J. Mamin, D. Rugar, and C. L. Degen, Spurious harmonic response of multipulse quantum sensing sequences, Phys. Rev. X **5**, 021009 (2015).

[14] R. J. D. Tilley, *Color Centers* (Springer, New York, 2014), pp. 1–9.

[15] E. V. Levine, M. J. Turner, P. Kehayias, C. A. Hart, N. Langellier, R. Trubko, D. R. Glenn, R. R. Fu, and R. L. Walsworth, Principles and techniques of the quantum diamond microscope, Nanophotonics **8**, 1945 (2019).

[16] S. Pezzagna and J. Meijer, Quantum computer based on color centers in diamond, Appl. Phys. Rev. **8**, 011308 (2021).

[17] R. L. Fagaly, Superconducting quantum interference device instruments and applications, Rev. Sci. Instrum. **77**, 101101 (2006).

[18] M. W. Doherty, N. B. Manson, P. Delaney, F. Jelezko, J. Wrachtrup, and L. C. L. Hollenberg, The nitrogen-vacancy colour centre in diamond, Phys. Rep. **528**, 1 (2013).

[19] A. Gruber, A. Dräbenstedt, C. Tietz, L. Fleury, J. Wrachtrup, and C. von Borczyskowski, Scanning confocal optical microscopy and magnetic resonance on single defect centers, Science **276**, 2012 (1997).

[20] F. Jelezko, T. Gaebel, I. Popa, A. Gruber, and J. Wrachtrup, Observation of coherent oscillations in a single electron spin, Phys. Rev. Lett. **92**, 076401 (2004).

[21] J. H. N. Loubser and J. A. van Wyk, Electron spin resonance in the study of diamond, Rep. Prog. Phys. **41**, 1201 (1978).

[22] L. Rondin, J.-P. Tetienne, T. Hingant, J.-F. Roch, P. Maletinsky, and V. Jacques, Magnetometry with nitrogen-vacancy defects in diamond, Rep. Prog. Phys. **77**, 056503 (2014).

[23] C. P. Slichter, *Principles of Magnetic Resonance*, Springer Series in Solid-State Sciences Vol. 1 (Springer, Berlin, 1996).

[24] J. T. Oon, J. Tang, C. A. Hart, K. S. Olsson, M. J. Turner, J. M. Schloss, and R. L. Walsworth, Ramsey envelope modulation in NV diamond magnetometry, Phys. Rev. B **106**, 054110 (2022).

[25] Y. Azuma, S. Nomura, H. Watanabe, and S. Kashiwaya, Angle dependence of ^{15}N nuclear spin dynamics in diamond NV centers, arXiv:2306.07556.

[26] H. J. Mamin, M. H. Sherwood, M. Kim, C. T. Rettner, K. Ohno, D. D. Awschalom, and D. Rugar, Multipulse double-quantum magnetometry with near-surface nitrogen-vacancy centers, Phys. Rev. Lett. **113**, 030803 (2014).

[27] P. London, P. Balasubramanian, B. Naydenov, L. P. McGuinness, and F. Jelezko, Strong driving of a single spin using arbitrarily polarized fields, Phys. Rev. A **90**, 012302 (2014).

[28] C. Müller, Sensing single spins with colour centres in diamond, Ph.D. thesis, Universität Ulm, 2016.

[29] F. Campaioli, J. H. Cole, and H. Hapuarachchi, Quantum master equations: Tips and tricks for quantum optics, quantum computing, and beyond, PRX Quantum **5**, 020202 (2024).

[30] J. R. Johansson, P. D. Nation, and F. Nori, QuTiP: An open-source Python framework for the dynamics of open quantum systems, Comput. Phys. Commun. **183**, 1760 (2012).

[31] J. R. Johansson, P. D. Nation, and F. Nori, QuTiP 2: A Python framework for the dynamics of open quantum systems, Comput. Phys. Commun. **184**, 1234 (2013).

[32] D. Manzano, A short introduction to the Lindblad master equation, AIP Adv. **10**, 025106 (2020).

[33] K. Volkova, J. Heupel, S. Trofimov, F Betz, R. Colom, R. W. MacQueen, S. Akhundzada, M. Reginka, A. Ehresmann, J. P. Reithmaier, S. Burger, C. Popov, and B. Naydenov, Optical and spin properties of NV center ensembles in diamond nanopillars, Nanomaterials **12**, 1516 (2022).

[34] I. Panadero, H. Espinós, L. Tsunaki, K. Volkova, A. Tobalina, J. Casanova, P. Acedo, B. Naydenov, R. Puebla, and E. Torrontegui, Photon-emission statistics for single nitrogen-vacancy centers, Phys. Rev. Appl. **22**, 014035 (2024).

[35] G. Balasubramanian, I. Y. Chan, R. Kolesov, M. Al-Hmoud, J. Tisler, C. Shin, C. Kim, A. Wojcik, P. R. Hemmer, A. Krueger *et al.*, Nanoscale imaging magnetometry with diamond spins under ambient conditions, Nature (London) **455**, 648 (2008).

[36] J. M. Binder, A. Stark, N. Tomek, J. Scheuer, F. Frank, K. D. Jahnke, C. Müller, S. Schmitt, M. H. Metsch, T. Unden, T. Gehring, A. Huck, U. L. Andersen, L. J. Rogers, and F. Jelezko, Qudi: A modular python suite for experiment control and data processing, SoftwareX **6**, 85 (2017).

[37] L. Tsunaki *et al.*, Quantum color centers analysis toolbox (QuaCCAToo) (2024), https://github.com/QISS-HZB/QuaCCAToo.

[38] J. L. Rodgers and W. Alan Nicewander, Thirteen ways to look at the correlation coefficient, Am. Stat. **42**, 59 (1988).

[39] B. A. Myers, Quantum decoherence of near-surface nitrogen-vacancy centers in diamond and implications for nanoscale imaging, Ph.D. thesis, University of California, Santa Barbara, 2016.

[40] L. G. Rowan, E. L. Hahn, and W. B. Mims, Electron-spin-echo envelope modulation, Phys. Rev. **137**, A61 (1965).

[41] N. Zhao, J. Honert, B. Schmid, M. Klas, J. Isoya, M. Markham, D. Twitchen, F. Jelezko, R.-B. Liu, H. Fedder *et al.*, Sensing single remote nuclear spins, Nat. Nanotechnol. **7**, 657 (2012).

[42] J. Scheuer, I. Schwartz, S. Müller, Q. Chen, I. Dhand, M. B. Plenio, B. Naydenov, and F. Jelezko, Robust techniques for polarization and detection of nuclear spin ensembles, Phys. Rev. B **96**, 174436 (2017).

[43] J. Scheuer and B. Naydenov, *Dynamic Nuclear Polarization (DNP) in Diamond* (Elsevier, Amsterdam, 2020).

[44] A. P. Nizovtsev, S. Y. Kilin, A. L. Pushkarchuk, V. A. Pushkarchuk, and F. Jelezko, Theoretical study of hyperfine interactions and optically detected magnetic resonance spectra by simulation of the $C_{291}[NV]^{-}H_{172}$ diamond cluster hosting nitrogen-vacancy center, New J. Phys. **16**, 083014 (2014).

[45] A. Dréau, J.-R. Maze, M. Lesik, J.-F. Roch, and V. Jacques, High-resolution spectroscopy of single NV defects coupled with nearby ^{13}C nuclear spins in diamond, Phys. Rev. B **85**, 134107 (2012).

[46] B. Smeltzer, L. Childress, and A. Gali, ^{13}C hyperfine interactions in the nitrogen-vacancy centre in diamond, New J. Phys. **13**, 025021 (2011).

[47] Z.-Y. Wang, J. E. Lang, S. Schmitt, J. Lang, J. Casanova, L. McGuinness, T. S. Monteiro, F. Jelezko, and M. B. Plenio, Randomization of pulse phases for unambiguous and robust quantum sensing, Phys. Rev. Lett. **122**, 200403 (2019).

[48] J. F. Haase, Z.-Y. Wang, J. Casanova, and M. B. Plenio, Pulse-phase control for spectral disambiguation in quantum sensing protocols, Phys. Rev. A **94**, 032322 (2016).

[49] Z. Wang, J. Casanova, and M. B. Plenio, Enhancing the robustness of dynamical decoupling sequences with correlated random phases, Symmetry **12**, 730 (2020).

[50] J. Casanova, Z.-Y. Wang, I. Schwartz, and M. B. Plenio, Shaped pulses for energy-efficient high-field NMR at the nanoscale, Phys. Rev. Appl. **10**, 044072 (2018).

[51] L. Tsunaki, Dataset for ambiguous resonances in multipulse quantum sensing with NVs (2024), https://figshare.com/articles/dataset/Dataset_for_Ambiguous_Resonances_in_Multipulse_Quantum_Sensing_with_NVs/26245895.